ACS APPLIED MATERIALS & INTERFACES

www.acsami.org

Research Article

Plasma-Made Graphene Nanostructures with Molecularly Dispersed F and Na Sites for Solar Desalination of Oil-Contaminated Seawater with Complete In-Water and In-Air Oil Rejection

Shenghao Wu, Biyao Gong, Huachao Yang, Yikuan Tian, Chenxuan Xu, Xinzheng Guo, Guoping Xiong, Tengfei Luo, Jianhua Yan, Kefa Cen, Zheng Bo,* Kostya Ken Ostrikov, and Timothy S. Fisher

Cite This: https://dx.doi.org/10.1021/acsami.0c07921

Read Online

ACCESS | Metrics & More | Article Recommendations | Supporting Information

ABSTRACT: Solar desalination that exploits interfacial evaporation represents a promising solution to global water scarcity. Real-world feedstocks (*e.g.*, natural seawater and contaminated water) include oil contamination issues, raising a compelling need for desalination systems that offer anti-oil-fouling capability; however, it is still challenging to prepare oil-repellent and meanwhile water-attracting surfaces. This work demonstrates a concept of molecularly dispersing functional F and Na sites on plasma-made vertically oriented graphene nanosheets to achieve an in-air and in-water oleophobic, hydrophilic surface. The graphene architecture presents high in-air (138°) and in-water (145°) oil contact angles, with simultaneously high water affinity (0°). Such surface wettability is enabled by oleophobic, hydrophobic $-CF_x$, and hydrophilic −COONa groups of the molecules that disperse on graphene surfaces; low-dispersion (0.439 mJ m^{-2}) and high-polarity (95.199 mJ m^{-2}) components of the solid surface tension; and increased surface roughness produced by graphene edges. The graphene nanostructures pump water upward by capillary action but repel oil from the surface, leading to complete in-water and in-air oil rejection and universal anti-oil-fouling capability for solar desalination. Consequently, stable solar−vapor energy efficiency of more than 85% is achieved regardless of whether the feedstock is pure or oil-contaminated water (*e.g.*, a mixture of oil floating on water, an oil-in-water emulsion), resulting in the efficient production of clean water over several days. This outstanding performance is attributed to the universal (both in-water and in-air) oleophobic wettability, together with high light absorptance contributed by nanotraps, fast interfacial heat transfer enhanced by finlike nanostructures, and accelerated evaporation enabled by sharp graphene edges.

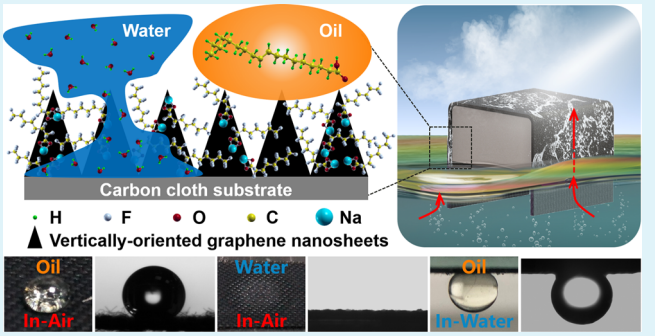

KEYWORDS: *solar−thermal energy, plasma-made nanostructures, in-air and in-water oleophobicity, molecular dispersion, solar evaporation, water desalination*

Water scarcity, driven by constantly increasing economic development and global environmental pollution, has elicited much demand for new, technology-driven solutions.[1−3] Solar desalination, based on evaporating seawater using solar energy to produce clean water, represents a promising solution to the global water scarcity.[4] Conventional desalination systems typically heat the entire bulk liquid, leading to significant heat losses to the environment by conduction, convection, and radiation.[5] Recently, a solar-driven interfacial evaporation method, based on locally heating the water−air interface by solar−thermal conversion, was proposed and it reduced the heat loss to less than 15%.[6,7] This efficient solar desalination approach was further advanced by subsequent works and enhanced *via* improved evaporating materials and optimized structures.[8−21] However, prior work has typically used pure water and/or artificially saline water as the feedstocks in testing solar-evaporating performance. Conversely, feedstocks in real-world conditions, such as natural seawater and contaminated water collected from urban waterways, are more complicated and require additional progress to improve the antifouling behavior of the evaporating surface.[22−27]

Oil is a typical contaminant in natural seawater and urban waterways due to industrial and residential effluents.[28−31] Oil causes severe fouling issues when oil-containing water is used as the feedstock in solar desalination systems.[32] As shown in Figure S1, a typical solar absorber made of carbonized wood possesses an oleophilic, hydrophilic surface. When the

Received: April 30, 2020
Accepted: July 13, 2020
Published: July 13, 2020

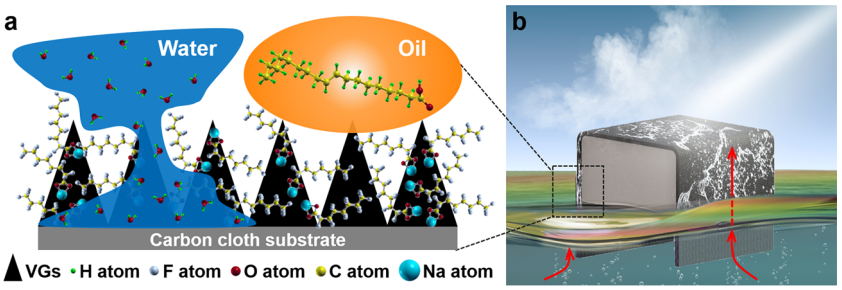

Figure 1. Design of an oleophobic, hydrophilic surface by dispersing fluorinated molecules on graphene nanostructures to achieve anti-oil-fouling solar desalination. (a) Schematic of dispersing fluorinated molecules on graphene surfaces. (b) Schematic of anti-oil-fouling solar desalination. The oil (rainbow-colored) is afloat on the seawater surface (dark green).

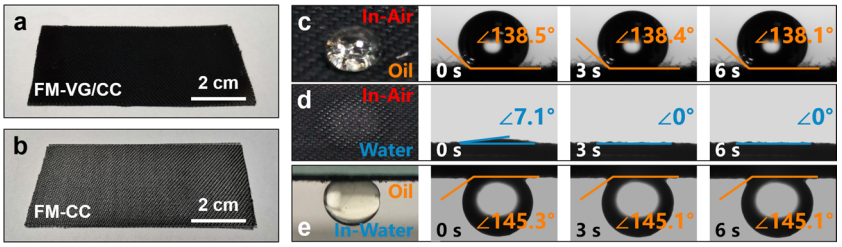

Figure 2. Surface wettability characterization. (a) Optical images of an FM-VG/CC sample. (b) Optical images of a fluorinated-molecule-coated carbon cloth (FM-CC) sample. (c) Oil contact angle in the air. (d) Water contact angle in the air. (e) Oil contact angle under water.

carbonized wood floats on the oil−water mixture, oil migrates to the wood surface. Upon exposure to solar illumination, water is heated by the carbonized wood and then evaporates. However, to escape from the evaporating surface, the water vapor must permeate through the oil layer, which impedes the release of water vapor to the environment. As a result, the evaporation flux (0.55 kg m^{-2} h^{-1}) decreases dramatically compared with systems fed with pure water (1.26 kg m^{-2} h^{-1}), leading to a large reduction in solar−vapor energy efficiency (<40%).

Recent work has drawn attention to these oil-fouling issues and developed underwater oleophobic surfaces to address the fouling issues caused by the oil dispersed in water, *e.g.*, oil-in-water emulsions.[23,33] Nevertheless, such underwater oleophobic surfaces may become oleophilic when exposed to air, thus failing to prevent oil fouling. Moreover, in real-world applications, oil exists in water (*e.g.*, oil-in-water emulsions), floats on the water surface (*e.g.*, floating oil layers), and even splatters from the environment. Therefore, practical desalination solutions require further advances. Developing an in-water and simultaneously in-air oleophobic, hydrophilic surface represents a promising solution to address the oil-fouling challenge. Usually, an oil-repellent surface with extremely low surface tension is more likely to repel water because the surface tension of water (72.8 mJ m^{-2}) is much higher than that of oil (commonly <30 mJ m^{-2}).[34] As such, a universal oleophobic, hydrophilic surface is attractive but very challenging to prepare. In earlier works, external stimuli, such as moisture, electricity, and ammonia vapor, were applied to achieve temporary oleophobicity/hydrophilicity.[35−37] Subsequent works developed various surface engineering methods to obtain durable oleophobic/hydrophilic surfaces. Li et al. fabricated nanometer-thick polymer networks that are more wettable to water than to oil.[38,39] Pan et al. developed a fluorinated nanoparticle coating to make oil-repellent/water-spreading surfaces.[34,40] Lin et al. employed a chemical coating method to prepare oleophobic/hydrophilic fabrics.[41] Nevertheless, such oil-repellent and simultaneously water-attracting surfaces need further development to satisfy practical applications, *e.g.*, solar desalination.

The present work demonstrates an in-water and simultaneously in-air oleophobic, hydrophilic surface by dispersing functional molecules on vertically oriented graphene nanosheets (VGs) to realize an anti-oil-fouling solar desalination system. As shown in Figure 1, VGs (black triangles) are perpendicularly oriented on a carbon cloth substrate (gray) by plasma-enhanced chemical vapor deposition (PECVD). The VGs are purposely introduced to enhance light absorptance and solid−liquid interfacial heat transfer, as well as to increase the surface roughness to improve the anti-oil-fouling behavior. Fluorinated molecules (FMs, sodium perfluorooctanoate, $C_7F_{15}COONa$) that possess both oleophobic, hydrophobic $-CF_x$ and hydrophilic −COONa groups are uniformly dispersed on graphene nanosheets, thus achieving simultaneously in-air and in-water (termed for simplicity universal below) oleophobicity and hydrophilic wettability. As a result, water wets the graphene structures, while oil is repelled from the surface. The oleophobic, hydrophilic graphene architecture is applied to solar-driven interfacial evaporation and exhibits a durable anti-oil-fouling ability with complete in-water and in-air oil rejection. Stable solar−vapor conversion efficiency of more than 85% is achieved regardless of whether the feedstock is pure or oil-contaminated water (*e.g.*, a mixture of oil floating on water, an oil-in-water emulsion), leading to the long-term efficient production of clean water over several days.

RESULTS AND DISCUSSION

Surface Wettability Characterization. An in-water and simultaneously in-air oleophobic, hydrophilic surface is achieved by growing VGs on commercial carbon cloth, followed by dispersing fluorinated molecules on the graphene surfaces. The VGs are synthesized by a customized PECVD system based on 13.56 MHz inductively coupled plasmas (ICPs) operated in a tubular reactor geometry. A piece of

https://dx.doi.org/10.1021/acsami.0c07921
ACS Appl. Mater. Interfaces XXXX, XXX, XXX−XXX

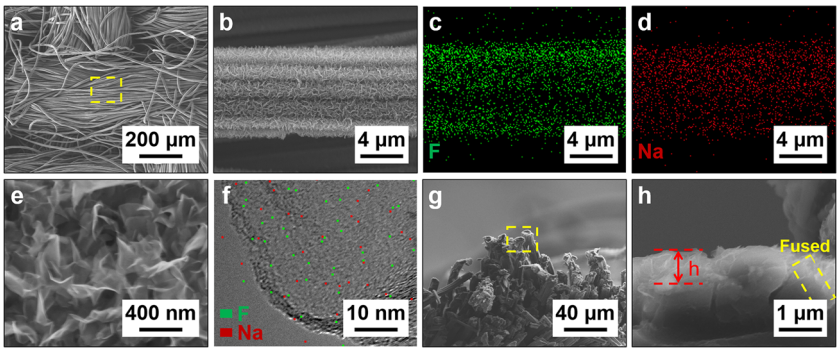

Figure 3. Molecular dispersion on graphene nanosheets. (a, b) Top-view SEM images of an FM-VG/CC sample. (c) EDS mapping image of fluorine. (d) EDS mapping image of sodium. (e) Top-view high-magnification SEM image. (f) High-magnification TEM image integrating EDS elemental mapping results. The color dots were expanded and highlighted to make them more visible. (g, h) Cross-sectional SEM images of the FM-VG/CC sample.

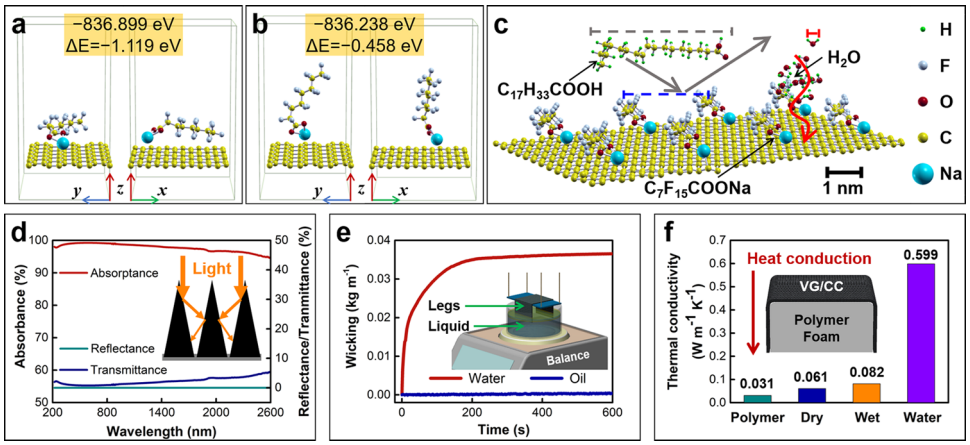

Figure 4. DFT calculations and material characterizations. (a) Relaxed structure of DFT conformation 1 with the carbon backbone nearly parallel to the graphene plane. (b) Relaxed structure of DFT conformation 2 with the carbon backbone nearly perpendicular to the graphene plane. (c) Mechanistic illustration of H_2O (water) and $C_{17}H_{33}COOH$ (oil) penetrating through the $C_7F_{15}COONa$ layer. (d) Photonic properties of the FM-VG/CC film. (e) Wicking measurements of the FM-VG/CC film. (f) Characterization of thermal conductivities.

carbon cloth (CC) sheet (with a thickness of 0.32 mm) is used as the substrate for the growth of VGs, producing a graphene-based hybrid structure (denoted VG/CC). Subsequently, fluorinated molecules are dispersed to the VGs through immersion in ethanol solution and then dried at room environment to obtain the final product (denoted FM-VG/CC). As shown in Figure 2a, the FM-VG/CC sample presents a black surface caused by the growth of VGs. In contrast, a fluorinated-molecule-coated carbon cloth sample presents a gray surface (see Figure 2b).

The surface wettability of the FM-VG/CC has been measured. As shown in Figure 2c, when an oil droplet is placed on the sample in the air, it maintains a large contact angle (>138°), suggesting in-air oleophobicity. As shown in Figure 2d, when a water droplet contacts the FM-VG/CC surface, it quickly permeates into the sample, indicating in-air hydrophilicity. As shown in Figure 2e, when the FM-VG/CC sample is immersed in water, the oil contact angle increases to 145°, showing in-water oleophobic wettability. Such universal oleophobic wettability is purposely designed to address oil fouling issues in desalination systems, which can occur in both air and water environments. Meanwhile, the hydrophilic surface can serve as a capillary pump to supply water in the desalination process, which will be described below.

Molecular Dispersion of Functional Sites on Graphene Nanosheets. One of the key factors in realizing simultaneous in-air and in-water oleophobicity and hydrophilicity is the layer of fluorinated molecules covering graphene nanosheets. As shown in the scanning electron microscopy (SEM) images in Figure 3a–e, graphene nanosheets are uniformly distributed on the interlaced fibers of carbon cloth whose diameters range from several to tens of microns. These fibers are composed of elemental carbon and maintain the interlaced structures well during the PECVD process (see the comparison with the SEM images of bare carbon cloth in Figure S2). Fluorine-containing functional groups ($-CF_3$ and $-CF_2$) and polar end groups ($-COONa$) are introduced by coating the $C_7F_{15}COONa$ molecules on graphene surfaces. As shown by X-ray photoelectron spectroscopy (XPS) in Figure S3, a fluorine peak is observed after the coating process. Subsequently, energy-dispersive X-ray spectroscopy (EDS) is used to observe the elemental distributions, as shown in Figure 3c,d. The EDS elemental maps reveal that fluorine sites and sodium sites are evenly distributed on the sample surface. In a high-magnification image (see Figure 3f) obtained by transmission electron microscopy (TEM), it is observed that green dots (F) and red dots (Na) are sparsely dispersed on the graphene nanosheets.

https://dx.doi.org/10.1021/acsami.0c07921
ACS Appl. Mater. Interfaces XXXX, XXX, XXX−XXX

Density functional theory (DFT) calculations were conducted to explore the possible conformations of the fluorinated molecule absorbed on the graphene surface. Five conformations with the $C_7F_{15}COONa$ molecule carbon backbone parallel to (conformation 1, see Figure 4a), perpendicular to (conformation 2 with the −COONa group inward to, see Figure 4b; conformation 3 with the −COONa group outward from, see Figure S4a), and tilted away from (conformation 4, see Figure S4b; conformation 5, see Figure S4c) a single-layer graphene surface are created. All conformations were relaxed based on energy minimization. Note that van der Waals interaction proposed by Langreth and Lundqvist groups was included during the relaxation process.[42] The details of the calculations setup and relaxed atomic positions are available in Note S4. The Gibbs free energy of conformation 1 is calculated to be −836.899 eV, which is lower than those of conformation 2 (−836.238 eV), conformation 3 (−835.730 eV), conformation 4 (−836.549 eV), and conformation 5 (−836.447 eV). Conformation 1 presents the lowest Gibbs free energy and thus is considered as the most stable one among the five, also indicating the high probability of existence.

As shown in Figure 4a, the $C_7F_{15}COONa$ carbon backbone of conformation 1 is nearly parallel to the graphene plane, which is slightly different from the descriptions in prior literature.[34,40] Although a schematic was shown to illustrate the absorption conformation in the prior reports, in which the $C_7F_{15}COONa$ carbon backbone was nearly perpendicular to metal−oxide substrates (that was similar to conformation 2 in the current work), the prior work did not explain the detailed mechanism.[34,40] Consequently, the absorption mechanism remains unclear. In the current work, the angle and direction of the $C_7F_{15}COONa$ carbon backbone to the graphene substrate are varied and compared based on DFT calculations. Because there are no effective means to experimentally visualize individual molecules, we must rely on the DFT results and believe that conformation 1 is the most populated among the five. It is worth noting that other, higher-energy states can become populated at higher temperatures. The conformation of the absorbed fluorinated molecule might also largely depend on the property of the solid surface (*e.g.*, graphene, TiO_2, or Al_2O_3) and the interaction between the molecule and surface atoms.[43]

Indeed, the F sites (*i.e.*, $-CF_3$ and $-CF_2$ groups) of the $C_7F_{15}COONa$ molecule are both oleophobic and hydrophobic, by which both oil and water should be repelled.[38,39] These fluorine-containing groups create high-density intermolecular voids that serve as filters to separate small water molecules and large oil molecules. As shown in Figure 4c, the water molecules (*i.e.*, H_2O) are intrinsically much smaller than the oil molecules (*e.g.*, oleic acid, $C_{17}H_{33}COOH$, which is a major constituent of canola oil) so that it is possible to tune the intermolecular voids to allow the penetration of small water molecules while preventing the penetration of large oil molecules.[38] Usually, a higher packing density of the F sites leads to smaller intermolecular voids that result in higher resistance for oil penetration. The detailed elucidation is available in Note S6. Thus, by engineering the $C_7F_{15}COONa$ molecule layer, water can pass through the voids, while oil is precluded. Moreover, the Na sites (*i.e.*, polar −COONa groups) have a high affinity to water and can facilitate the penetrated water molecules to wet the solid surface. Furthermore, there are no functional groups on the graphene surface that are particularly attractive to the nonpolar oil molecules. Additionally, a wettability test using a VG/CC sample without a fluorinated coating was performed and exhibited an oleophilic, hydrophobic nature (see Figure S6). The wettability comparison between the samples with and without the fluorinated coating further clarifies the functions of the molecular sites.

Unique Wettability Enabled by Tuning Solid Surface Tension. The simultaneous oleophobic and hydrophilic characteristics can be explained by Owens−Wendt's surface energy theory, in which surface tension balances the sum of the dispersion and polarity force components.[44,45] Young's equation can be written as

$$\cos\theta = \frac{2\sqrt{\gamma_s^d \gamma_l^d} + 2\sqrt{\gamma_s^p \gamma_l^p}}{\gamma_l^d + \gamma_l^p} - 1 \quad (1)$$

where θ is the contact angle, γ_s^d and γ_s^p are the dispersion and polarity components of the solid surface tension, respectively, and γ_l^d and γ_l^p are the dispersion and polarity components of the liquid (water and oil, respectively) surface tension. γ_s^d is measured to be 0.439 mJ m^{-2}, while γ_s^p is measured to be 95.199 mJ m^{-2} (see the measurement method in Note S8) for the FM-VG/CC sample. Because both γ_s^d and the polarity components (γ_{oil}^p) of oil are close to zero, we find that $\cos\theta \rightarrow -1$, *i.e.*, $\theta \rightarrow 180°$ for oil. On the one hand, the dual oleophobic, hydrophobic fluorine-containing groups ($-CF_3$ and $-CF_2$) only make small contributions to γ_s^d and γ_s^p, while the γ_s^d of the −COONa group is small too. On the other hand, the polar −COONa groups result in a high γ_s^p.[34,40] Therefore, the fluorinated molecules (with low γ_s^d and high γ_s^p) coupled by bimodal sites can attract polar molecules (like water) and meanwhile repel nonpolar molecules (like oil).

Increased Surface Roughness Produced by Graphene Edges. Our results suggest that surface roughness is also a critical factor for the observed in-air oleophobicity. To increase the surface roughness, nanoparticles, such as TiO_2, Al_2O_3, were previously used.[34,40] The effect of surface roughness can be explained by the Wenzel relation[46]

$$\cos\theta^* = r\cos\theta \quad (2)$$

where r is the roughness factor of a solid surface, θ is the contact angle of a smooth surface, and θ^* is the contact angle of a rough surface. If $r = 1$, the solid surface is smooth; if $r > 1$, the surface is rough. As such, increasing the surface roughness can lead to increased surface wettability, which means an oleophobic surface can be more oleophobic ($\theta^* > \theta > 90°$).

In the current work, the rough surface is achieved by introducing VGs that own sharp, exposed, and high-density graphene edges. As shown in the high-magnification SEM image of Figure 3e, the VGs present wall-like, interconnected nanosheets (with a span ranging from 200 to 400 nm), open channels, and exposed graphene edges. In contrast, the surface of bare carbon cloth fibers is smooth, as shown by the SEM images in Figure S2. Meanwhile, atomic force microscopy (AFM) analysis was applied to quantitively evaluate the surface roughness (see details in Note S9). In the three-dimensional (3D) AFM image of a bare carbon cloth sample, the surface in a 2 μm × 2 μm area is a plane with a height variation smaller than 30 nm (see Figure S8a). Correspondingly, the root-mean-square roughness (R_{rms}) of this flat surface is calculated to be 2.78 nm. On the contrary, the 3D AFM image of the FM-VG/CC film shows a significant surface height variation of 99.7 nm (see Figure S8b). The R_{rms} is then calculated to be 14.05 nm, which is five-fold higher than that of the bare carbon cloth

https://dx.doi.org/10.1021/acsami.0c07921
ACS Appl. Mater. Interfaces XXXX, XXX, XXX−XXX

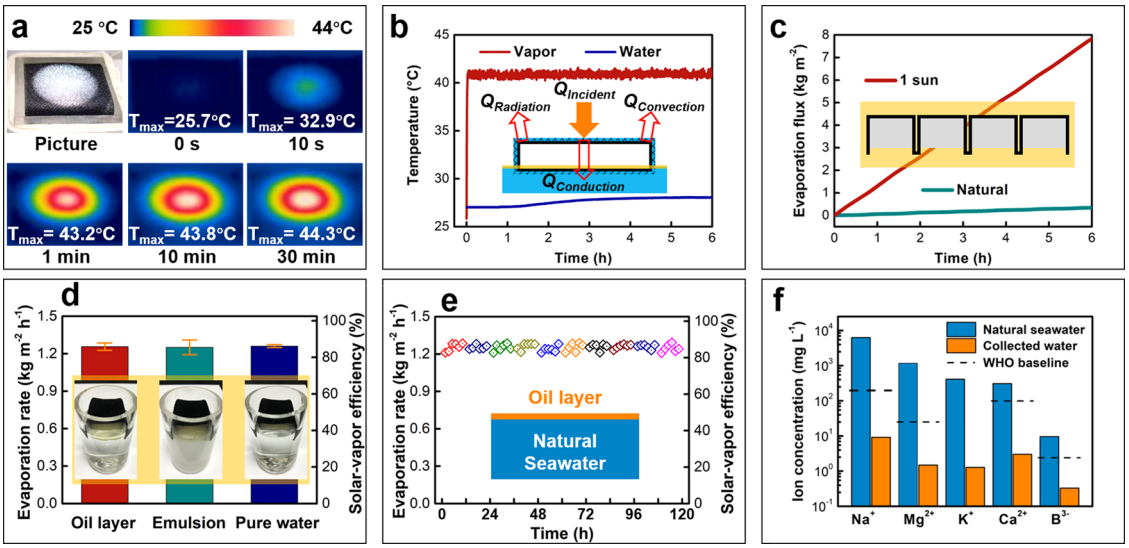

Figure 5. Solar-driven interfacial evaporation performance. (a) Infrared images of temperature evolution on the evaporating surface. (b) Temperature evolution of the hot vapor (red) and the pool water (blue). (c) Evaporation flux under solar illumination of 1 sun (red) and natural evaporation (green) in a dark environment. (d) Comparison of evaporation performance using different feedstocks including a mixture of oil floating on water, an oil-in-water emulsion, and pure water. (e) Solar desalination fed by oil-contaminated natural seawater. (f) Ion concentrations in the condensed, collected water compared with those in the oil-contaminated natural seawater.

sample (2.78 nm). Thus, the surface roughness can be increased by VGs. On the other hand, the wettability of a fluorinated-molecule-coated carbon cloth sample was tested and exhibited an in-air oil contact angle of 131° (see Figure S9), lower than that of the FM-VG/CC sample (138°). The comparison further supports that the in-air oleophobic wettability is enhanced by increasing surface roughness. Note that the coating process does not change the morphology since the molecules (<2 nm) are far smaller than the VGs, as evidenced by the comparison of SEM images with VG/CC (see Figure S10).

Moreover, the surface roughness is very stable because of the chemical bonding between the VGs and the carbon cloth. As shown in the cross-sectional SEM images of Figure 3g,h, the VGs extend from the hosting structures (*i.e.*, carbon fibers), forming a fused, mechanically stable junction. According to our prior work, the junction formation is attributed to chemical bonds formed upon exposure to energetic plasma species and produces a mechanically robust connection between the VGs and substrates in practical applications (*e.g.*, solar desalination and oil-spill recovery).[47,48] The dense graphene nanosheets grow perpendicularly on the surface of hosting structures and possess a typical height from hundreds of nanometers to microns. Furthermore, the unique, oriented structures and open channels are favorable for building light traps to increase light absorption.[12,47]

Characterization of the FM-VG/CC Nanostructures. The optical properties including reflectance (R) and transmittance (T) have been experimentally measured. The absorptance (A) is calculated by $A = 1 - R - T$. As shown in Figure 4d, the FM-VG/CC sample exhibits high absorptance across a broad wavelength range from 200 to 2600 nm, which covers the most energetic part of the solar spectrum (*i.e.*, ultraviolet−visible−near-infrared region). The average absorptance is calculated to be 97.65%, which means only 2.35% of light is reflected from or transmits through FM-VG/CC. Meanwhile, the absorptance of a VG/CC sample without fluorination is measured to be 98.03% (see Figure S11a). A carbon cloth sample with a fluorinated coating shows an absorptance of 85.63% (see Figure S11b). The results indicate that the fluorinated coating slightly reduces the absorptance (from 98.03 to 97.65%), but the reduction is small. The high light absorptance is mainly attributed to the VG growth. The roles of VGs in harvesting light have been systematically studied in our prior work.[47,49] The unique orientation that is nearly paralleled to the direction of the incident light and the wall-like structures enhance light trapping, as schematically shown in the inset of Figure 4d. When light reaches the open graphene channels, it undergoes multiple reflections inside the nanotraps until it is completely absorbed by the graphene nanosheets.

In solar desalination applications, a thin FM-VG/CC film covers a polystyrene foam, forming the solar evaporator (see Figure 1b). Two FM-VG/CC film legs insert into the underneath liquid (*e.g.*, water, oil, and oil−water mixture) and serve as water-wicking paths to pump water upward by the capillary. Since water is repelled by the hydrophobic polymer foam and can only flow through the FM-VG/CC film, a two-dimensional (2D) waterway is created. Importantly, sufficient water supply is crucial for evaporation applications and is now demonstrated by a wicking test (see the inset in Figure 4e). The wicking mass is monitored by a precision balance and divided by the total width of the two legs (40 mm × 2 mm). More details on the experimental setup are available in Note S13. As shown by the red curve in Figure 4e, when the FM-VG/CC sample contacts water, the water-wicking mass increases quickly within the first 200 s and eventually plateaus at 0.037 kg m^{-1}. The half-saturated wicking rate (calculated by fitting the data from 16 to 180 s) is calculated to be 0.331 kg m^{-1} h^{-1}. Assuming the length of the evaporation area to be w, the area wicking rate is $0.331/w$ kg m^{-2} h^{-1}. In the current work, w is 0.04 m. On the other hand, when the FM-VG/CC sample contacts oil, the two legs float on the oil surface due to the repulsion from oil. The oil wicking mass always remains zero (see the blue curve in Figure 4e), indicating the complete oil rejection. Therefore, the FM-VG/CC film has the ability to

https://dx.doi.org/10.1021/acsami.0c07921
ACS Appl. Mater. Interfaces XXXX, XXX, XXX−XXX

separate water from the oil−water mixture and then deliver the water upward. Additional results using oil−water mixtures are summarized in Figure S12.

In addition to wicking behavior, top-down thermal conduction is another important factor in interfacial evaporation performance. The heat generated by solar−thermal conversion is localized at the water−air interface by hindering the top-down thermal conduction. As shown in the inset of Figure 4f, the effective top-down thermal conductivity of the evaporator with 2D waterways has been measured. The effective thermal conductivity at the dry state is 0.0609 W m^{-1} K^{-1}, which is greater than that of a bare polymer foam (0.0311 W m^{-1} K^{-1}). Thereafter, the FM-VG/CC sample was wetted by water before the measurement to simulate a working condition (*i.e.*, evaporating with a wet surface). The effective thermal conductivity at the wet state was measured to be 0.0818 W m^{-1} K^{-1}, which is slightly higher than that at the dry state but still far lower than that of water (0.599 W m^{-1} K^{-1}). Thus, such an FM-VG/CC−polymer evaporator can efficiently insulate against top-down heat conduction from the water−air interface.

Solar-Driven Interfacial Evaporation. Solar-driven interfacial evaporation tests have been conducted using the FM-VG/CC−polymer composite. An oil−water mixture was produced by adding canola oil on the water surface and used as a feedstock. Simulated solar light with a diameter of 3 cm and an average intensity of 1 kW m^{-2} illuminate the top surface of the FM-VG/CC film. The thin FM-VG/CC film with two legs inserted into the oil−water mixture absorbs light and converts it to thermal energy. Then, the water is heated by the FM-VG/CC surface, generating water vapor at the water−air interface. The FM-VG/CC surface temperature is recorded by an infrared camera. The vapor temperature (at ∼2 mm above the center of the FM-VG/CC film) and the pool water temperature (at ∼5 mm below the bottom of the polymer foam) are monitored by thermocouples with a diameter of ∼0.3 mm.

As shown in Figure 5a, when exposed to 1 sun irradiation, the surface temperature quickly increases to 43.2 °C in the first 1 min and then gradually reaches a plateau of 44.0 ± 0.3 °C. As shown in Figure 5b, the vapor temperature (red curve) rapidly increases at a rate of 0.23 °C s^{-1} in the first 1 min and then fluctuates around 40.87 ± 0.20 °C. In contrast, the pool water temperature (blue curve) changes slowly. After 6 h of continuous evaporation, only a small increase of 1.02 °C in temperature is observed. This result suggests that conductive heat loss to the bulk water is small, confirming the excellent top-down insulating performance. The real-time evaporation flux is monitored by a precision balance. As shown in Figure 5c, the evaporation flux increases smoothly, indicating good process stability. The measured evaporation rate is linearly fitted to be 1.314 ± 0.030 kg m^{-2} h^{-1}, while the real evaporation rate over 6 h is calculated to be 1.256 ± 0.030 kg m^{-2} h^{-1} after subtracting natural evaporation (0.058 kg m^{-2} h^{-1}). The solar−vapor energy conversion efficiency is calculated based on

$$H_{\text{solar-vapor}} = m_{\text{evap}}(h_{\text{lv}} + C\,(T_{\text{v}} - T_{\text{l}}))/q_i \quad (3)$$

where m_{evap} is the real evaporation rate (in the unit of kg m^{-2} s^{-1}), h_{lv} is the temperature-dependent latent heat (2403.86 kJ kg^{-1} at 40.85 °C when assuming the partial pressure of water vapor equal to saturated pressure at a certain temperature) for liquid−vapor phase change, C is the specific heat of liquid water (4.2 kJ kg^{-1} K^{-1}, assuming no sensible heating of the vapor), T_{v} is the average vapor temperature (40.85 °C) over 6 h, T_{l} is the average water temperature (27.64 °C) over 6 h, and q_i is the incident solar intensity (*i.e.*, 1 kW m^{-2}). $\eta_{\text{solar-vapor}}$ is calculated to be 85.81 ± 2.05%. The thermal analysis was conducted based on a simplified model (see calculations in Note S14), as shown in the inset of Figure 5b. It is estimated that 1.8% of the energy dissipates to the pool bulk liquid through top-down heat conduction ($Q_{\text{conduction}}$), 3.1% of the heat dissipates by convection ($Q_{\text{convection}}$), and 2.2−12.3% dissipates through radiation ($Q_{\text{radiation}}$) to the surroundings (in which the maximum and minimum limits correspond to the hot vapor and air, respectively). This range is reasonable since the total loss is 7.1−17.2% given the overall solar to vapor efficiency (85.81%). A rational energy balance between the input energy (*i.e.*, 976 W m^{-2} from light) and the estimated output energy (*i.e.*, 929−1030 W m^{-2} to heat) is obtained in the current system.

Efficient solar-driven evaporation can be attributed to several factors. First, high light absorptance (97.65%) is the result of the VGs with open channels, wall-like structures, and exposed edges to create high-density light traps. Second, the excellent top-down thermal insulation produced by combining the external FM-VG/CC layer and the internal low-conductance polymer foam leads to very little heat leakage from the top surface to the bulk liquid, which is prone to dissipating heat to the environment. Third, the interfacial heat transfer is enhanced by finlike graphene nanosheets to increase the effective interface area.[25,47,50] Consequently, the heat generated in VGs can transfer to the surrounding water with high efficiency. Finally, sharp VG edges provide abundant tips at the solid−liquid−air three-phase contact lines. These tips may facilitate the water molecules to escape from liquid to air, enabling fast evaporation.[51]

Additional solar evaporation tests fed by oil−water emulsion and pure water have been conducted and compared, as shown in Figure 5d. When fed by an oil−water emulsion, the real evaporation rate and solar−vapor efficiency are measured to be 1.251 ± 0.059 kg m^{-2} h^{-1} and 85.46 ± 4.03%, respectively. When fed by pure water, the real evaporation rate and solar−vapor efficiency are measured to be 1.261 ± 0.012 kg m^{-2} h^{-1} and 86.15 ± 0.82%, respectively. The detailed measurements of the evaporation fluxes are available in Note S15. Apparently, the FM-VG/CC architecture is able to maintain high solar evaporation performance regardless of whether the feedstock is pure water or oil-contaminated water. These results further confirm the excellent anti-oil-fouling capability of our engineered material. It is worth noting that when assuming that all vapor is generated at room temperature (*i.e.*, 25 °C with a latent heat of 2441.5 kJ kg^{-1}, which is the minimum energy used for the phase change of water without heating for temperature increase),[17] the upper limit of evaporation rate at 1 sun is calculated to be 1.475 kg m^{-2} h^{-1} at 25 °C. In the above wicking test, the amount of water supplied by the wicking legs is measured to be 0.331 kg m^{-1} h^{-1}. To ensure the sufficient water supply for evaporation at 1 sun, the length (l) of the evaporating area should suffice: $2 \times 0.331 \times w > 1.475 \times l \times w$, where w is the width of evaporation area (*i.e.*, the width of two wicking legs). Thus, l is suggested to be no more than 0.45 m. In the current work, l is 0.04 m, indicating the sufficient water supply. In future scalable applications, we expect to drill holes in the polymer foam and insert more wicking legs, as shown in the inset of Figure 5c, to ensure

https://dx.doi.org/10.1021/acsami.0c07921
ACS Appl. Mater. Interfaces XXXX, XXX, XXX−XXX

sufficient water supply. Assuming a 10 m × 10 m evaporation surface is equipped with a solar desalination system in Los Angeles, California that has abundant solar energy (with an average monthly global horizontal irradiance of 5.3 kWh m^{-2} day^{-1}) but suffers from water stress,[52] nearly 68 000 gallons of clean water will be produced for 1 year.

Solar Desalination with Oil-Contaminated Natural Seawater. The FM-VG/CC architecture has been further applied to solar desalination at 1 sun. Natural seawater collected from the South China Sea (20.0 °N 110.1 °E) was used without pretreatment, with a thin layer of canola oil added on the surface. During the desalination process, water evaporates, while nonvolatile salts reside on the surface of the FM-VG/CC film. The salt residues usually present white color that reduces light absorption and thus degrades the evaporation performance. Due to the accumulation of salt, the ion concentration on the evaporating surface increases to become higher than that of the underlying seawater. Interestingly, the dissoluble salt ions spontaneously diffuse from a high-concentration region to a relatively low-concentration region due to the concentration gradient. As a result, when the FM-VG/CC film freely floats on seawater, the white salt spots gradually disappear because of ion diffusion from the FM-VG/CC film to the underneath liquid, which is noted as a self-salt-cleaning process. When the solar simulator is turned on, white salts gradually accumulate on the evaporating surface, are first observed at the second hour, and then slowly grow as time prolongs further (see Figure S15a). When the solar simulator is turned off at the sixth hour, the self-salt-cleaning begins. As shown in Figure S15b, the white salt spots become smaller and smaller and completely disappear at the 11th hour. To avoid the negative effect of salt accumulation on long-term performance, the duration of continuous evaporation is set as 6 h to simulate practical desalination in daylight hours (assuming 6 h under normal solar irradiation), followed by 6 h of self-salt-cleaning that simulates free floating during night hours. Thus, each cycle consists of 12 h, and the long-term test consists of 10 cycles, corresponding to 120 h.

As shown in Figure 5e, the hourly evaporation rate fluctuates from 1.208 to 1.293 kg m^{-2} h^{-1} without obvious performance degradation. Subsequently, hot vapor/condensed water is collected by a transparent quartz dome. Ion concentrations were detected and are shown in Figure 5f. The concentrations of Na^+, Mg^+, K^+, Ca^{2+}, and B^{3-} in the collected water are measured to be 9.21, 1.49, 1.29, 3.01, and 0.33 mg L^{-1}, respectively, all of which meet the World Health Organization (WHO) drinking water standards (200, 25, 100, and 2.4 mg L^{-1} for Na^+, Mg^{2+}, Ca^{2+}, and B^{3-}, respectively),[53,54] and are dramatically lower than those in the natural seawater (6331, 1177, 413, 311, and 9.6 mg L^{-1} for Na^+, Mg^+, K^+, Ca^{2+}, and B^{3-}, respectively). This result shows that the ions existing in natural seawater are efficiently separated from the hot vapor/condensed water. Moreover, reusability is another important feature in practical applications. After the desalination process, the oil contact angle of the FM-VG/CC film shows a small decline but is still greater than 120° (see Figure S17), indicating stable and reproducible oleophobicity. However, the slow deterioration could become dramatic after months or years of operation. A feasible method to remediate the deteriorated wettability is to recoat the $C_7F_{15}COONa$ layer after long-term operations. As shown in Figure S17, the oil contact angle rebounds to 140° after employing the coating process again. More details are available in Note S17.

CONCLUSIONS

An in-air and in-water oleophobic, hydrophilic surface is devised by dispersing functional F and Na sites on graphene nanosheets. The fabricated FM-VG/CC graphene architecture shows high in-air (~138°) and in-water (~145°) oil contact angles and simultaneously high water affinity (0°). Such surface wettability is attributed to the following factors: (1) oleophobic, hydrophobic F sites ($-CF_x$ groups), and hydrophilic Na sites (−COONa groups) can preclude large oil molecules from traversing and meanwhile allow small water molecules penetrating through the $C_7F_{15}COONa$ molecule layer; (2) the low-dispersion (0.439 mJ m^{-2}) and high-polarity (95.199 mJ m^{-2}) components of the solid surface tension lead to the repulsion of nonpolar oil molecules and the attraction of polar water molecules; and (3) the increased surface roughness produced by high-density graphene edges further enhance the in-air oleophobicity.

The in-air and in-water oleophobic, hydrophilic graphene architecture is applied for solar desalination and presents a universal anti-oil-fouling ability with complete oil rejection. Consequently, stable solar−vapor energy efficiency of more than 85% is achieved regardless of whether the feedstock is pure or oil-contaminated water (*e.g.*, a mixture of oil floating on water, an oil-in-water emulsion), resulting in the efficient production of clean water over several days. The reliable performance is attributed to the universal (both in-water and in-air) oleophobic wettability, together with high light absorptance near 98% contributed by nanotraps, low top-down thermal conductivity (0.0609 W m^{-1} K^{-1} at a dry state and 0.0818 W m^{-1} K^{-1} at a wet state) engineered by 2D waterways, fast interfacial heat transfer enhanced by finlike nanostructures, and accelerated evaporation enabled by sharp graphene edges.

EXPERIMENTAL SECTION

PECVD Growth. Commercial carbon cloth (with a thickness of 0.32 ± 0.02 mm) was used as the substrate of graphene nanosheets in a customized inductively coupled plasma-enhanced chemical vapor deposition (ICP-PECVD) system. In a typical procedure, the carbon cloth with a plane size of 4 cm × 8 cm was placed in a cylindrical quartz tube, which was sealed and vacuumed to <10 Pa. Then, it was heated to 700 °C under the moderate-vacuum conditions, followed by gas flow injection of a mixture of CH_4 (5 mL min^{-1}) and H_2 (5 mL min^{-1}). Subsequently, the pressure was tuned to ~100 Pa and a radio frequency source of 250 W was coupled into the quartz tube to carry on the growth process. Finally, the VG/CC sample was extracted from the growth chamber after cooling down to room temperature under the protection of Ar flow (10 mL min^{-1}).

Coating of Fluorinated Molecules. Sodium perfluorooctanoate ($C_7F_{15}COONa$, 97%) was purchased from Alfa Aesar. An ethanol solution (0.1 M) was prepared by adding $C_7F_{15}COONa$ powders to ethanol (99.5%), following by magnetically stirring and naturally cooling to room temperature. The solid sample was immersed in the as-prepared solution for 30 min and then dried at the room environment overnight to obtain the fluorinated-molecule-coated samples.

DFT Calculations. The Vienna *ab initio* simulation package (VASP) is used for the DFT calculations under generalized gradient approximation (GGA) and Perdew−Burke−Ernzerhof (PBE) functions.[55−58] The self-consistent field and force convergence criteria are set as 1 × 10^{-5} eV and 1 × 10^{-4} eV $Å^{-1}$, respectively. An energy cutoff of 520 eV is used, and the spin polarization is considered for all

https://dx.doi.org/10.1021/acsami.0c07921
ACS Appl. Mater. Interfaces XXXX, XXX, XXX−XXX

calculations. The Gaussian smearing method with a width of 0.05 eV is employed to determine electron occupancies. Van der Waals corrections enabled by the DFT-D2 method are also incorporated to characterize the long-range interactions.[59] The *K*-point of 5 × 5 × 1 ($x \times y \times z$) is used. A vacuum space of more than 20 Å is used along the *z*-axis. All crystalline structures are visualized by XCrySDen.[60]

Material Characterization. The morphology was observed by SEM (SU-70, Hitachi) and TEM (JEM 2100F, JEOL). The surface wettability was characterized by an optical contact angle measuring instrument (DropMeter A-200). The photonic transmittance (T) and reflectance (R) were measured by an ultraviolet−visible−near-infrared spectrophotometer (UV-3150, Shimadzu) in which an integrating sphere was used. The elemental composition was detected by XPS (Escalab Mark II, VG) with a monochromatic Mg Kα X-ray source (1 253.6 eV). The surface roughness was measured by AFM (MultiMode, VEECO). The thermal conductivity was measured by a Hot Disk apparatus (TPS 2500 S, Hot Disk).

Solar-Driven Interfacial Evaporation Test. A solar simulator (PLS−SXE300D, Beijing Perfect Light Technology) equipped with a <5° collimated light source and an optical filter was used to obtain standard AM 1.5 G spectrum irradiation. An optical power meter (PL-MW2000, Beijing Perfect Light Technology) was used to monitor the solar intensity. An infrared camera (T1050sc, FLIR) was used to map the temperature distribution on the solid surface. Three T-type thermocouples with an accuracy of 0.01 °C and a silvery surface were used to measure the temperature of vapor and water. The mass flux was measured by a precision balance (CPA225D, Sartorius) with an accuracy of 0.01 mg. Canola oil was used. The oil-in-water emulsion was prepared by mixing 4 mL of canola oil and 100 mL of water in a beaker and then magnetically stirring for 12 h before solar-driven evaporation tests. All tests were conducted at the ambient temperature of ∼25 °C and an atmospheric pressure of ∼0.1 MPa, with a humidity of ∼53%. Error bars were derived from multiple sets of repeatable tests.

■ ASSOCIATED CONTENT

Supporting Information

The Supporting Information is available free of charge at https://pubs.acs.org/doi/10.1021/acsami.0c07921.

Significance and urgency to address oil-fouling issues (Note S1), SEM images of carbon cloth (Note S2), XPS characterization (Note S3), setup and relaxed structures of DFT calculations (Note S4), DFT conformations 3−5 (Note S5), elucidation of the effect of F site packing density on wettability (Note S6), surface wettability of a VG/CC sample without the fluorinated coating (Note S7), surface tension measurement (Note S8), AFM characterization (Note S9), surface wettability of a fluorinated-molecule-coated carbon cloth sample (Note S10), SEM images of VG/CC without the fluorinated coating (Note S11), comparison of photonic properties (Note S12), experimental setup of wicking tests (Note S13), analysis of the thermal balance (Note S14), evaporation flux measurement (Note S15), self-salt-cleaning test (Note S16), and reusability characterization of the FM-VG/CC film (Note S17) (PDF)

■ AUTHOR INFORMATION

Corresponding Author

Zheng Bo − *State Key Laboratory of Clean Energy Utilization, College of Energy Engineering and Hangzhou Global Scientific and Technological Innovation Center, Zhejiang University, Hangzhou, Zhejiang 310027, China;* orcid.org/0000-0001-9308-7624; Email: bozh@zju.edu.cn

Authors

Shenghao Wu − *State Key Laboratory of Clean Energy Utilization, College of Energy Engineering and Hangzhou Global Scientific and Technological Innovation Center, Zhejiang University, Hangzhou, Zhejiang 310027, China; Department of Mechanical & Aerospace Engineering and California NanoSystems Institute, University of California, Los Angeles, Los Angeles, California 90095, United States;* orcid.org/0000-0001-9083-0785

Biyao Gong − *State Key Laboratory of Clean Energy Utilization, College of Energy Engineering and Hangzhou Global Scientific and Technological Innovation Center, Zhejiang University, Hangzhou, Zhejiang 310027, China*

Huachao Yang − *State Key Laboratory of Clean Energy Utilization, College of Energy Engineering and Hangzhou Global Scientific and Technological Innovation Center, Zhejiang University, Hangzhou, Zhejiang 310027, China*

Yikuan Tian − *State Key Laboratory of Clean Energy Utilization, College of Energy Engineering and Hangzhou Global Scientific and Technological Innovation Center, Zhejiang University, Hangzhou, Zhejiang 310027, China*

Chenxuan Xu − *State Key Laboratory of Clean Energy Utilization, College of Energy Engineering and Hangzhou Global Scientific and Technological Innovation Center, Zhejiang University, Hangzhou, Zhejiang 310027, China*

Xinzheng Guo − *State Key Laboratory of Clean Energy Utilization, College of Energy Engineering and Hangzhou Global Scientific and Technological Innovation Center, Zhejiang University, Hangzhou, Zhejiang 310027, China*

Guoping Xiong − *Department of Mechanical Engineering, University of Nevada, Reno, Nevada 89557, United States*

Tengfei Luo − *Department of Aerospace and Mechanical Engineering, University of Notre Dame, Notre Dame, Indiana 46556, United States;* orcid.org/0000-0003-3940-8786

Jianhua Yan − *State Key Laboratory of Clean Energy Utilization, College of Energy Engineering and Hangzhou Global Scientific and Technological Innovation Center, Zhejiang University, Hangzhou, Zhejiang 310027, China*

Kefa Cen − *State Key Laboratory of Clean Energy Utilization, College of Energy Engineering and Hangzhou Global Scientific and Technological Innovation Center, Zhejiang University, Hangzhou, Zhejiang 310027, China*

Kostya Ken Ostrikov − *State Key Laboratory of Clean Energy Utilization, College of Energy Engineering, Zhejiang University, Hangzhou, Zhejiang 310027, China; School of Chemistry, Physics and Mechanical Engineering, Queensland University of Technology, Brisbane, Queensland 4000, Australia; Joint CSIRO-QUT Sustainable Processes and Devices Laboratory, Lindfield, NSW 2070, Australia;* orcid.org/0000-0001-8672-9297

Timothy S. Fisher − *Department of Mechanical & Aerospace Engineering and California NanoSystems Institute, University of California, Los Angeles, Los Angeles, California 90095, United States;* orcid.org/0000-0002-8909-313X

Complete contact information is available at: https://pubs.acs.org/10.1021/acsami.0c07921

Author Contributions

Z.B., S.W., K.(K.)O., and T.F. conceived the project and discussed on the conceptualization of the work and experimental designs. S.W., B.G., Y.T., and C.X. fabricated materials and performed experiments. S.W., H.Y., and X.G. conducted the simulations. Z.B., S.W., G.X., T.L., J.Y., K.C., K.

https://dx.doi.org/10.1021/acsami.0c07921
ACS Appl. Mater. Interfaces XXXX, XXX, XXX−XXX

(K.)O., and T.F. analyzed the data and interpreted the results. All of the authors contributed to the writing of the manuscript.

Notes

The authors declare no competing financial interest.

■ ACKNOWLEDGMENTS

This work is supported by the National Natural Science Foundation of China (grant number 51722604) and the Zhejiang Provincial Natural Science Foundation of China (grant number LR17E060002). Z.B. thanks the National Program for Support of Top-notch Young Professionals. S.W. acknowledges the support from the China Scholarship Council (grant number 201906320205), the 2019 Zhejiang University Academic Award for Outstanding Doctoral Candidates (grant number 2019029), Zhejiang University (grant number 419004A), and the University of California, Los Angeles. H.Y. acknowledges the support from the China Postdoctoral Science Foundation (grant number 2019M662048). G.X. acknowledges the support of the start-up funding from the University of Nevada, Reno. T.L. acknowledges the support from the National Science Foundation (grant numbers 1706039, 1937949). K.(K.)O. acknowledges the support from the Australian Research Council and the State Key Laboratory of Clean Energy Utilization Open Fund (grant numbers ZJUCEU2019002). S.W. thanks Qian Chen from Zhejiang University for assisting in experiments.

■ REFERENCES

(1) Gao, M. M.; Zhu, L. L.; Peh, C. K.; Ho, G. W. Solar Absorber Material and System Designs for Photothermal Water Vaporization Towards Clean Water and Energy Production. *Energy Environ. Sci.* **2019**, *12*, 841−864.

(2) Pulizzi, F.; Sun, W. J. Treating Water with Nano. *Nat. Nanotechnol.* **2018**, *13*, No. 633.

(3) Zhang, P. P.; Liao, Q. H.; Yao, H. Z.; Huang, Y. X.; Cheng, H. H.; Qu, L. T. Direct Solar Steam Generation System for Clean Water Production. *Energy Storage Mater.* **2019**, *18*, 429−446.

(4) Zhou, L.; Tan, Y.; Wang, J.; Xu, W.; Yuan, Y.; Cai, W.; Zhu, S.; Zhu, J. 3d Self-Assembly of Aluminium Nanoparticles for Plasmon-Enhanced Solar Desalination. *Nat. Photonics* **2016**, *10*, 393−398.

(5) Tao, P.; Ni, G.; Song, C. Y.; Shang, W.; Wu, J. B.; Zhu, J.; Chen, G.; Deng, T. Solar-Driven Interfacial Evaporation. *Nat. Energy* **2018**, *3*, 1031−1041.

(6) Ghasemi, H.; Ni, G.; Marconnet, A. M.; Loomis, J.; Yerci, S.; Miljkovic, N.; Chen, G. Solar Steam Generation by Heat Localization. *Nat. Commun.* **2014**, *5*, No. 4449.

(7) Wang, Z.; Liu, Y. M.; Tao, P.; Shen, Q. C.; Yi, N.; Zhang, F. Y.; Liu, Q. L.; Song, C. Y.; Zhang, D.; Shang, W.; Deng, T. Bio-Inspired Evaporation through Plasmonic Film of Nanoparticles at the Air-Water Interface. *Small* **2014**, *10*, 3234−3239.

(8) Jiang, Q.; Tian, L.; Liu, K.-K.; Tadepalli, S.; Raliya, R.; Biswas, P.; Naik, R. R.; Singamaneni, S. Bilayered Biofoam for Highly Efficient Solar Steam Generation. *Adv. Mater.* **2016**, *28*, 9400−9407.

(9) Zhou, X. Y.; Zhao, F.; Guo, Y. H.; Zhang, Y.; Yu, G. H. A Hydrogel-Based Antifouling Solar Evaporator for Highly Efficient Water Desalination. *Energy Environ. Sci.* **2018**, *11*, 1985−1992.

(10) Li, X.; Xu, W.; Tang, M.; Zhou, L.; Zhu, B.; Zhu, S.; Zhu, J. Graphene Oxide-Based Efficient and Scalable Solar Desalination under One Sun with a Confined 2d Water Path. *Proc. Natl. Acad. Sci. U.S.A* **2016**, *113*, 13953−13958.

(11) Zhang, P.; Li, J.; Lv, L.; Zhao, Y.; Qu, L. Vertically Aligned Graphene Sheets Membrane for Highly Efficient Solar Thermal Generation of Clean Water. *ACS Nano* **2017**, *11*, 5087−5093.

(12) Ren, H.; Tang, M.; Guan, B.; Wang, K.; Yang, J.; Wang, F.; Wang, M.; Shan, J.; Chen, Z.; Wei, D.; Peng, H.; Liu, Z. Hierarchical Graphene Foam for Efficient Omnidirectional Solar-Thermal Energy Conversion. *Adv. Mater.* **2017**, *29*, No. 1702590.

(13) Li, Y.; Gao, T.; Yang, Z.; Chen, C.; Luo, W.; Song, J.; Hitz, E.; Jia, C.; Zhou, Y.; Liu, B.; Yang, B.; Hu, L. 3d-Printed, All-in-One Evaporator for High-Efficiency Solar Steam Generation under 1 Sun Illumination. *Adv. Mater.* **2017**, *29*, No. 1700981.

(14) Wang, J.; Li, Y.; Deng, L.; Wei, N.; Weng, Y.; Dong, S.; Qi, D.; Qiu, J.; Chen, X.; Wu, T. High-Performance Photothermal Conversion of Narrow-Bandgap Ti2o3 Nanoparticles. *Adv. Mater.* **2016**, *29*, No. 1603730.

(15) Xu, N.; Hu, X.; Xu, W.; Li, X.; Zhou, L.; Zhu, S.; Zhu, J. Mushrooms as Efficient Solar Steam-Generation Devices. *Adv. Mater.* **2017**, *29*, No. 1606762.

(16) Yang, P. H.; Liu, K.; Chen, Q.; Li, J.; Duan, J. J.; Xue, G. B.; Xu, Z. S.; Xie, W. K.; Zhou, J. Solar-Driven Simultaneous Steam Production and Electricity Generation from Salinity. *Energy Environ. Sci.* **2017**, *10*, 1923−1927.

(17) Liu, Z.; Song, H.; Ji, D.; Li, C.; Cheney, A.; Liu, Y.; Zhang, N.; Zeng, X.; Chen, B.; Gao, J.; Li, Y.; Liu, X.; Aga, D.; Jiang, S.; Yu, Z.; Gan, Q. Extremely Cost-Effective and Efficient Solar Vapor Generation under Nonconcentrated Illumination Using Thermally Isolated Black Paper. *Global Challenges* **2017**, *1*, No. 1600003.

(18) Li, Y.; Gao, T.; Yang, Z.; Chen, C.; Kuang, Y.; Song, J.; Jia, C.; Hitz, E. M.; Yang, B.; Hu, L. Graphene Oxide-Based Evaporator with One-Dimensional Water Transport Enabling High-Efficiency Solar Desalination. *Nano Energy* **2017**, *41*, 201−209.

(19) Yi, L.; Ci, S.; Luo, S.; Shao, P.; Hou, Y.; Wen, Z. Scalable and Low-Cost Synthesis of Black Amorphous Al-Ti-O Nanostructure for High-Efficient Photothermal Desalination. *Nano Energy* **2017**, *41*, 600−608.

(20) Yang, Y.; Zhao, R.; Zhang, T.; Zhao, K.; Xiao, P.; Ma, Y.; Ajayan, P. M.; Shi, G.; Chen, Y. Graphene-Based Standalone Solar Energy Converter for Water Desalination and Purification. *ACS Nano* **2018**, *12*, 829−835.

(21) Pang, Y. S.; Zhang, J. J.; Ma, R. M.; Qu, Z. G.; Lee, E.; Luo, T. F. Solar-Thermal Water Evaporation: A Review. *ACS Energy Lett.* **2020**, *5*, 437−456.

(22) Ni, G.; Zandavi, S. H.; Javid, S. M.; Boriskina, S. V.; Cooper, T. A.; Chen, G. A Salt-Rejecting Floating Solar Still for Low-Cost Desalination. *Energy Environ. Sci.* **2018**, *11*, 1510−1519.

(23) Ma, Q. L.; Yin, P. F.; Zhao, M. T.; Luo, Z. Y.; Huang, Y.; He, Q. Y.; Yu, Y. F.; Liu, Z. Q.; Hu, Z. N.; Chen, B.; Zhang, H. Mof-Based Hierarchical Structures for Solar-Thermal Clean Water Production. *Adv. Mater.* **2019**, *31*, No. 1808249.

(24) Xia, Y.; Hou, Q. F.; Jubaer, H.; Li, Y.; Kang, Y.; Yuan, S.; Liu, H. Y.; Woo, M. W.; Zhang, L.; Gao, L.; Wang, H. T.; Zhang, X. W. Spatially Isolating Salt Crystallisation from Water Evaporation for Continuous Solar Steam Generation and Salt Harvesting. *Energy Environ. Sci.* **2019**, *12*, 1840−1847.

(25) Wu, S. H.; Xiong, G. P.; Yang, H. C.; Gong, B. Y.; Tian, Y. K.; Xu, C. X.; Wang, Y.; Fisher, T.; Yan, J. H.; Cen, K. F.; Luo, T. F.; Tu, X.; Bo, Z.; Ostrikov, K. Multifunctional Solar Waterways: Plasma-Enabled Self-Cleaning Nanoarchitectures for Energy-Efficient Desalination. *Adv. Energy Mater.* **2019**, *9*, No. 1901286.

(26) Zhu, B.; Kou, H.; Liu, Z. X.; Wang, Z. J.; Macharia, D. K.; Zhu, M. F.; Wu, B. H.; Liu, X. G.; Chen, Z. G. Flexible and Washable Cnt-Embedded Pan Nonwoven Fabrics for Solar-Enabled Evaporation and Desalination of Seawater. *ACS Appl. Mater. Interfaces* **2019**, *11*, 35005−35014.

(27) Zhang, P. P.; Liao, Q. H.; Zhang, T.; Cheng, H. H.; Huang, Y. X.; Yang, C.; Li, C.; Jiang, L.; Qu, L. T. High Throughput of Clean Water Excluding Ions, Organic Media, and Bacteria from Defect-Abundant Graphene Aerogel under Sunlight. *Nano Energy* **2018**, *46*, 415−422.

(28) Ma, Q. L.; Cheng, H. F.; Fane, A. G.; Wang, R.; Zhang, H. Recent Development of Advanced Materials with Special Wettability for Selective Oil/Water Separation. *Small* **2016**, *12*, 2186−2202.

(29) Li, Y. Q.; Zhang, H.; Fan, M. Z.; Zheng, P. T.; Zhuang, J. D.; Chen, L. H. A Robust Salt-Tolerant Superoleophobic Alginate/

https://dx.doi.org/10.1021/acsami.0c07921
ACS Appl. Mater. Interfaces XXXX, XXX, XXX−XXX

Graphene Oxide Aerogel for Efficient Oil/Water Separation in Marine Environments. *Sci. Rep.* **2017**, *7*, No. 46379.
(30) Ma, W. C.; Liu, B.; Zhang, R. X.; Gu, T. B.; Ji, X.; Zhong, L.; Chen, G. Y.; Ma, L. L.; Cheng, Z. J.; Li, X. P. Co-Upgrading of Raw Bio-Oil with Kitchen Waste Oil through Fluid Catalytic Cracking (Fcc). *Appl. Energy* **2018**, *217*, 233−240.
(31) Wu, S.; Yang, H.; Xiong, G.; Tian, Y.; Gong, B.; Luo, T.; Fisher, T. S.; Yan, J.; Cen, K.; Bo, Z.; Ostrikov, K. K. Spill-Sos: Self-Pumping Siphon-Capillary Oil Recovery. *ACS Nano* **2019**, *13*, 13027−13036.
(32) Al Malek, S. A.; Mohamed, A. M. O. Environmental Impact Assessment of Off Shore Oil Spill on Desalination Plant. *Desalination* **2005**, *185*, 9−30.
(33) Gong, B. Y.; Yang, H. C.; Wu, S. H.; Xiong, G. P.; Yan, J. H.; Cen, K. F.; Bo, Z.; Ostrikov, K. Graphene Array-Based Anti-Fouling Solar Vapour Gap Membrane Distillation with High Energy Efficiency. *Nano-Micro Lett.* **2019**, *11*, No. 51.
(34) Li, F. R.; Bhushan, B.; Pan, Y. L.; Zhao, X. Z. Bioinspired Superoleophobic/Superhydrophilic Functionalized Cotton for Efficient Separation of Immiscible Oil-Water Mixtures and Oil-Water Emulsions. *J. Colloid Interface Sci.* **2019**, *548*, 123−130.
(35) Kota, A. K.; Kwon, G.; Choi, W.; Mabry, J. M.; Tuteja, A. Hygro-Responsive Membranes for Effective Oil-Water Separation. *Nat. Commun.* **2012**, *3*, No. 1025.
(36) Kwon, G.; Kota, A. K.; Li, Y. X.; Sohani, A.; Mabry, J. M.; Tuteja, A. On-Demand Separation of Oil-Water Mixtures. *Adv. Mater.* **2012**, *24*, 3666−3671.
(37) Xu, Z. G.; Zhao, Y.; Wang, H. X.; Wang, X. G.; Lin, T. A Superamphiphobic Coating with an Ammonia-Triggered Transition to Superhydrophilic and Superoleophobic for Oil-Water Separation. *Angew. Chem., Int. Ed.* **2015**, *54*, 4527−4530.
(38) Li, L.; Wang, Y. J.; Gallaschun, C.; Risch, T.; Sun, J. N. Why Can a Nanometer-Thick Polymer Coated Surface Be More Wettable to Water Than to Oil? *J. Mater. Chem.* **2012**, *22*, 16719−16722.
(39) Wang, Y. J.; Dugan, M.; Urbaniak, B.; Li, L. Fabricating Nanometer-Thick Simultaneously Oleophobic/Hydrophilic Polymer Coatings Via a Photochemical Approach. *Langmuir* **2016**, *32*, 6723−6729.
(40) Li, F. R.; Wang, Z. R.; Huang, S. C.; Pan, Y. L.; Zhao, X. Z. Flexible, Durable, and Unconditioned Superoleophobic/Superhydrophilic Surfaces for Controllable Transport and Oil-Water Separation. *Adv. Funct. Mater.* **2018**, *28*, No. 1706867.
(41) Zhou, H.; Wang, H. X.; Yang, W. D.; Niu, H. T.; Wei, X.; Fu, S. D.; Liu, S.; Shao, H.; Lin, T. Durable Superoleophobic-Superhydrophilic Fabrics with High Anti-Oil-Fouling Property. *RSC Adv.* **2018**, *8*, 26939−26947.
(42) Lee, K.; Murray, E. D.; Kong, L. Z.; Lundqvist, B. I.; Langreth, D. C. Higher-Accuracy Van Der Waals Density Functional. *Phys. Rev. B* **2010**, *82*, No. 081101.
(43) Luo, T. F.; Lloyd, J. R. Molecular Dynamics Study of Thermal Transport in Gaas-Self-Assembly Monolayer-Gaas Junctions with Ab Initio Characterization of Thiol-Gaas Bonds. *J. Appl. Phys.* **2011**, *109*, No. 034301.
(44) Fowkes, F. M. Attractive Forces at Interfaces. *Ind. Eng. Chem.* **1964**, *56*, 40−52.
(45) Owens, D. K.; Wendt, R. C. Estimation of the Surface Free Energy of Polymers. *J. Appl. Polym. Sci.* **1969**, *13*, 1741−1747.
(46) Quéré, D. Wetting and Roughness. *Annu. Rev. Mater. Res.* **2008**, *38*, 71−99.
(47) Wu, S.; Xiong, G.; Yang, H.; Tian, Y.; Gong, B.; Wan, H.; Wang, Y.; Fisher, T. S.; Yan, J.; Cen, K.; Bo, Z.; Ostrikov, K. Scalable Production of Integrated Graphene Nanoarchitectures for Ultrafast Solar-Thermal Conversion and Vapor Generation. *Matter* **2019**, *1*, 1017−1032.
(48) Yu, K. H.; Bo, Z.; Lu, G. H.; Mao, S.; Cui, S. M.; Zhu, Y. W.; Chen, X. Q.; Ruoff, R. S.; Chen, J. H. Growth of Carbon Nanowalls at Atmospheric Pressure for One-Step Gas Sensor Fabrication. *Nanoscale Res. Lett.* **2011**, *6*, No. 202.
(49) Bao, H.; Kumar, A.; Cai, Y.; Ji, Y.; Fisher, T. S.; Ruan, X. Optical Properties of Thin Graphitic Nanopetal Arrays. *J. Quant. Spectrosc. Radiat. Transfer* **2015**, *158*, 84−90.
(50) Wei, X. F.; Zhang, T.; Luo, T. F. Molecular Fin Effect from Heterogeneous Self-Assembled Monolayer Enhances Thermal Conductance across Hard-Soft Interfaces. *ACS Appl. Mater. Interfaces* **2017**, *9*, 33740−33748.
(51) Yang, J.; Pang, Y.; Huang, W.; Shaw, S. K.; Schiffbauer, J.; Pillers, M. A.; Mu, X.; Luo, S.; Zhang, T.; Huang, Y.; Li, G.; Ptasinska, S.; Lieberman, M.; Luo, T. Functionalized Graphene Enables Highly Efficient Solar Thermal Steam Generation. *ACS Nano* **2017**, *11*, 5510−5518.
(52) Solar Energy Analysis for Los Angeles, Ca. Solar Energy Local. 2020. https://www.solarenergylocal.com/states/california/los-angeles/.
(53) *Calcium and Magnesium in Drinking-Water: Public Health Significance*; World HealthOrganization, 2009. http://www.who.int/water_sanitation_health/publications/publication_9789241563550/en/.
(54) *Safe Drinking-Water from Desalination*; World Health Organization, 2011. http://www.who.int/water_sanitation_health/publications/desalination_guidance/en/.
(55) Kresse, G.; Furthmüller, J. Efficient Iterative Schemes for Ab Initio Total-Energy Calculations Using a Plane-Wave Basis Set. *Phys. Rev. B* **1996**, *54*, 11169−11186.
(56) Kresse, G.; Furthmüller, J. Efficiency of Ab-Initio Total Energy Calculations for Metals and Semiconductors Using a Plane-Wave Basis Set. *Comput. Mater. Sci.* **1996**, *6*, 15−50.
(57) Perdew, J. P.; Chevary, J. A.; Vosko, S. H.; Jackson, K. A.; Pederson, M. R.; Singh, D. J.; Fiolhais, C. Atoms, Molecules, Solids, and Surfaces: Applications of the Generalized Gradient Approximation for Exchange and Correlation. *Phys. Rev. B* **1992**, *46*, 6671−6687.
(58) Perdew, J. P.; Burke, K.; Ernzerhof, M. Generalized Gradient Approximation Made Simple. *Phys. Rev. Lett.* **1996**, *77*, 3865−3868.
(59) Grimme, S. Semiempirical Gga-Type Density Functional Constructed with a Long-Range Dispersion Correction. *J. Comput. Chem.* **2006**, *27*, 1787−1799.
(60) Kokalj, A. Xcrysden - a New Program for Displaying Crystalline Structures and Electron Densities. *J. Mol. Graphics Modell.* **1999**, *17*, 176−179.

https://dx.doi.org/10.1021/acsami.0c07921
ACS Appl. Mater. Interfaces XXXX, XXX, XXX−XXX